

Associated production of Higgs and single top at the LHC in presence of the SMEFT operators

Subhaditya Bhattacharya,^a Sanjoy Biswas,^b Kuntal Pal,^c Jose Wudka^c

^a*Department of Physics, Indian Institute of Technology Guwahati, Assam 781039, India*

^b*Department of Physics, Ramakrishna Mission Vivekananda Educational and Research Institute, Belur Math, Howrah 711202, India*

^c*Department of Physics and Astrophysics, University of California, Riverside, USA*

E-mail: subhab@iitg.ac.in, sanjoy.phy@gm.rkmvu.ac.in, kp1002@ucr.edu,
jose.wudka@ucr.edu

ABSTRACT: We analyse the single top production in association with the Higgs at the Large Hadron Collider (LHC) using Standard Model (SM) effective operators upto dimension six. We show that the presence of effective operators can significantly alter the existing bound on the top-Higgs Yukawa coupling. We analyse events at the LHC with 35.9 and 137(140) fb⁻¹ integrated luminosities using both cut-based and machine learning techniques to probe new physics (NP) scale and operator coefficients addressing relevant SM background reduction. The four fermi effective operator(s) that contribute to the signal, turn out to be crucial and a limit on the top-Higgs Yukawa interaction in presence of them is obtained from the present data and for future sensitivities.

KEYWORDS: Higgs production, Higgs properties, SMEFT

Contents

1	Introduction	1
2	EFT operators in context of thj production at the LHC	3
2.1	Constraints on EFT Operator coefficients	6
2.2	Validity of the EFT approximation	8
3	Limits using current LHC data	9
3.1	Model implementation and production cross-section	9
3.2	Event Analysis and simulation techniques	12
4	Upcoming sensitivities at LHC	16
4.1	Cut-based analysis	17
4.2	Machine learning techniques	20
5	Summary and Conclusions	24

1 Introduction

The discovery of the Higgs boson at the LHC completed the spectrum predicted by the Standard Model (SM). Although the measured properties of this 125 GeV scalar strongly favour those of the SM Higgs (corresponding to a weak isodoublet with $Y = 1/2$), we are yet to pin them down fully, with the data still allowing $\gtrsim O(10\%)$ 1σ differences (assuming Gaussian errors) from the SM predictions [1].

A statistically significant deviation of the Higgs couplings from the SM predictions would provide strong evidence of new physics (NP), which is often parameterized by the signal-strength coefficients κ_X , that take the value $\kappa_X = 1$ in the SM. Accordingly, most studies look for evidence of NP in deviations from this value. However, if NP is present, there is no reason to believe that its only (or main) effect will be to modify the κ_X , in general, the process used to measure the couplings κ_X will also be affected by other NP effects.

Therefore a general study of the experimental sensitivity to the κ_X must also include all possible NP effects relevant to the processes under consideration, which is often more significant than the modification of κ_X from its SM prediction. Taking into account these other NP effects can significantly alter the limits on κ_X ; ignoring them leads to limits on the κ_X that are relevant only for very limited types of NP.

The purpose of this note is to illustrate these issues and analyze their consequences for the special case of an LHC process that is well-suited to measure the Higgs-top quark signal strength κ_t which is not yet well constrained, $|\kappa_t| < 1.7$ at 95% C.L. (assuming no

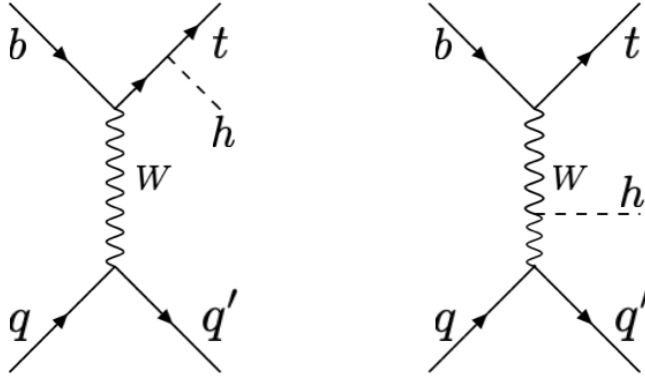


Figure 1. SM contributions to t -channel single-top production in association with a Higgs boson at the LHC.

other NP effects), and even its sign (relative to that of the $WW h$ coupling) is unknown [1]. The main channels through which the Higgs-top Yukawa coupling κ_t can be accessed are Higgs production via gluon fusion, $h t \bar{t}$ production, and $h \rightarrow \gamma\gamma$ decay. However, apart from $h \rightarrow \gamma\gamma$ decay, none of them are sensitive to the relative sign between $h t \bar{t}$ and $WW h$ couplings¹. Moreover, the gluon fusion and the $h t \bar{t}$ production receive significant higher order QCD corrections [3]; while the Higgs to photon decay process is suppressed since it is generated only at one loop.

These problems are not shared by Higgs production in association with single-top, which is sensitive to the magnitude and sign of κ_t [4, 5]. In the SM there are two relevant graphs (fig. 1), one proportional to κ_t and the other to the $h W W$ coupling $g_{h W W}$ ², so the cross-section will be particularly sensitive to the relative sign and magnitude of these two couplings. Moreover, the SM predicts that the two contributing diagrams will interfere destructively, making this process also sensitive to NP effects. In the following, we will study this process, which we refer to as thj (j denotes the light jet in the final state), as a probe of NP.

It was shown in [4, 5] that, absent any NP effects, the thj cross-section increases significantly when κ_t takes large negative values. The present LHC data also confirms the exclusion of $\kappa_t < -0.9$ [7]. The theoretical cross-section for thj production in the absence of other NP effects can be parametrized in terms of κ_t and κ_w at NLO using MADGRAPH5@MC@NLO [8] as follows,

$$\sigma_{thj} = (2.63\kappa_t^2 + 3.58\kappa_w^2 - 5.21\kappa_t\kappa_w)\sigma_{thj}^{\text{SM}}, \quad \kappa_w = \frac{g_{h W W}}{g_{h W W}^{\text{(SM)}}}. \quad (1.1)$$

σ_{thj}^{SM} at the LHC with $\sqrt{s} = 13$ TeV is 71 fb after using appropriate K factor of 1.187, as used by CMS analysis. In this analysis we consider all the effective (EFT) operators upto

¹Resolving the sign between hZZ and hWW couplings has been addressed in [2] and references therein.

²For constraints on the magnitude of $g_{h W W}$, see [6].

dimension six [9] that contribute to the thj production at LHC. Significant contribution arises only from those which are potentially tree generated (PTG) [10], while the operators that are loop generated (LG) suffer additional suppression and are neglected. Similar studies have been done in the context of one top quark and a pair of gauge boson production in [11, 12], for both thj and tZj processes at LHC including NLO corrections in [13], for finding the relative contribution of the operators that contribute to thj in [14]. A correlation between the operators that contribute to both $pp \rightarrow tHq$ and $pp \rightarrow tq$ has been performed in [15]. The change in the existing bound on κ_t in presence of these EFT operators, in particular the four fermi operator in context of the present LHC data and at future sensitivities are highlighted in the present work.

Our analysis involves state-of-the-art simulation techniques using both cut-based as well as machine learning (ML) analyses. We point out the key kinematic variables that are likely to segregate the signal including EFT operators from that of the SM background contamination. We set limits on the EFT operator coefficients, subject to the NP scale, which is likely to be excluded in future luminosities.

The paper is organized as follows: we discuss the EFT operators that contributes to thj production at LHC in section 2, bound on the EFT parameters from existing LHC data in section 3, signal significance and limits at future luminosities in section 4 and conclude in section 5.

2 EFT operators in context of thj production at the LHC

Assuming (as we will) that the NP is not directly observed, all NP effects are parameterized by a series of effective operators. It is well known [10] that there is no unique basis of such operators, but that all such bases are related through the equivalence theorem [16]; here we choose the so-called Warsaw basis [9]. Though we do not specify the details of the physics underlying the SM, we will assume that it is weakly coupled and decoupling.

Under these circumstances, it is relevant to differentiate operators according to whether they are generated at 1 or higher loops by the new physics (loop-generated or LG operators), or whether they can be generated at tree level (potentially tree-generated or PTG operators) [10]. This separation is useful because the Wilson coefficients of LG operators are necessarily suppressed by a factor³ $\sim 1/(4\pi)^2 \sim 0.006$, so that their effects will be generally negligible given the existing experimental precision⁴; in contrast, PTG operators can have $\mathcal{O}(1)$ Wilson coefficients. It is important to note that LG operators are loop generated by *any* kind of NP⁵, while PTG operators are generated at the tree level by at least one type of NP, though it may be that the NP realized in nature does not share

³This is the case, for example, for the operator (the notation is explained below eq. (2.1)) $W_{\mu\nu}^I(\bar{q}_t\sigma^{\mu\nu}\tau_I u_t)$ whose Wilson coefficient has a natural size of order $g/(4\pi\Lambda)^2$, *not* $1/\Lambda^2$.

⁴Ignoring this suppression often leads to the misleading conclusion that the effects of LG operators can be very important, but such results derive from assuming coefficients that deviate from their natural values by 3 or 4 orders of magnitude. There are, however, a few notable exceptions: SM processes that occur only at one loop, such as $h \rightarrow \gamma\gamma$; and reactions strongly suppressed by small CKM and PMNS matrix elements.

⁵Assuming this NP is described by a local gauge theory containing scalar, fermions and vector fields.

this property. Nonetheless, PTG operators offer the best opportunities for testing in the presence of a wide class of NP.

The SM quark-level amplitude leading to the thj final state are given in Fig. 1. When NP effects are included, the cross-section contains three terms: the pure SM contribution, an NP-SM interference term, and a pure NP term. Contributions involving NP will be suppressed by powers of the NP scale, which we denote by Λ ; for the case at hand the interference term is $\propto 1/\Lambda^2$ while the pure NP term is $\propto 1/\Lambda^4$. In our analysis, we have included both the interference, as well as the pure NP contribution. In section 3.2, we show the contribution of the EFT operators to thj production at different representative benchmark points within the parameter space scanned in the analysis. Dimension 8 operators, which also contribute $\propto 1/\Lambda^4$ via interference with SM, should, strictly speaking, be included – we expect, however, that such effects would be of similar order as the ones here obtained and would not change our conclusions; we will neglect them in the following analysis.

We are then interested in those effective operators that are PTG and can interfere with the SM amplitude in the thj process. It follows from the structure of the SM contribution that of the effective operators containing quarks, only those with left-handed light quarks (including the b) need be considered. With this in mind the operators we include are:

$$\begin{aligned}
\mathcal{O}_{\phi\Box} &= |\phi|^2 \Box |\phi|^2, \\
\mathcal{O}_{t\phi} &= |\phi|^2 (\bar{q}_t t_R \tilde{\phi}) + \text{H.c.}, \\
\mathcal{O}_{qq}^{(1)} &= (\bar{q}_t \gamma_\mu q_u) (\bar{q}_u \gamma^\mu q_t), \\
\mathcal{O}_{qq;1}^{(3)} &= (\bar{q}_t \gamma_\mu \tau^I q_t) (\bar{q}_u \gamma^\mu \tau^I q_u), \\
\mathcal{O}_{qq;2}^{(3)} &= (\bar{q}_t \gamma_\mu \tau^I q_u) (\bar{q}_u \gamma^\mu \tau^I q_t), \\
\mathcal{O}_{\phi q}^{(3)} &= (\bar{q}_t \tau^I \gamma^\mu q_t) (\phi^\dagger i \tau^I D_\mu \phi) + \text{H.c.} \quad (2.1)
\end{aligned}$$

where ϕ denotes the SM scalar doublet; q_t, q_u the top-bottom and up-down left-handed quark doublets, respectively; t_R the right-handed top singlet; and τ^I the Pauli matrices. We also note that there are two additional 4-fermions operators that contribute to the process of interest and interfere with the SM, but these are Fierz-equivalent to the ones listed (see section 2.2).

The relevant effective Lagrangian is then

$$\begin{aligned}
\mathcal{L}_{\text{eff}} &= \frac{C_h}{\Lambda^2} \mathcal{O}_{\phi\Box} + \frac{C_t}{\Lambda^2} \mathcal{O}_{u\phi} + \frac{1}{\Lambda^2} \left[C_{qq}^{(1)} \mathcal{O}_{qq}^{(1)} + C_{qq;1}^{(3)} \mathcal{O}_{qq;1}^{(3)} + C_{qq;2}^{(3)} \mathcal{O}_{qq;2}^{(3)} \right] + \frac{C_w}{\Lambda^2} \mathcal{O}_{\phi q}^{(3)} + \text{H.c.}; \\
&= \frac{2C_h v^2}{\Lambda^2} h \Box h + \frac{C_t v^2}{\sqrt{2} \Lambda^2} h (\bar{t} t) + \frac{C_{4f}}{\Lambda^2} \left[(\bar{d}_L \gamma_\mu u_L) (\bar{t}_L \gamma^\mu b_L) + \text{H.c.} \right] \\
&\quad + \frac{\sqrt{2} g C_w}{\Lambda^2} (h + v)^2 \left(\bar{t}_L \not{W}^+ b_L + \text{H.c.} \right); \quad (2.2)
\end{aligned}$$

where we assumed the operator coefficients are real and

$$C_{4\mathbf{f}} = \frac{1}{3}C_{qq}^{(1)} + 2C_{qq;1}^{(3)} - \frac{1}{3}C_{qq;2}^{(3)}. \quad (2.3)$$

A few comments are in order:

- The term $\propto C_{\mathbf{t}}$ modifies the top Yukawa coupling: $m_{\mathbf{t}}/\mathbf{v} \rightarrow (m_{\mathbf{t}}/\mathbf{v})\kappa_{\mathbf{t}}$ with $\kappa_{\mathbf{t}} = 1 - C_{\mathbf{t}}\mathbf{v}^3/(\sqrt{2}\Lambda^2 m_{\mathbf{t}})$; in the current context the top-quark signal strength for the Higgs is then $\kappa_{\mathbf{t}} \simeq 1 - C_{\mathbf{t}}(250 \text{ GeV}/\Lambda)^2$. Investigations (see *e.g.* [7]) that place limits on the value of $\kappa_{\mathbf{t}}$ without considering any other possible NP effects are *de facto* ignoring all but $\mathcal{O}_{t\phi}$ contributions. It is also worth noting that for natural values, $C_{\mathbf{t}} = \mathcal{O}(1)$, and $\Lambda > 1.5 \text{ TeV}$, $|\kappa_{\mathbf{t}} - 1| \lesssim 0.03$, which gives the precision required to probe physics beyond the electroweak scale associated with $\mathcal{O}_{t\phi}$.
- The term $\propto C_{\mathbf{w}}$ introduces $Wtbh$ and $Wtbh^2$ interactions, and also modifies the Wtb coupling, which now becomes $(g/\sqrt{2})(1 + 2C_{\mathbf{w}}\mathbf{v}^2/\Lambda^2)$; current (3- σ) limits on the t lifetime then imply $\Lambda/\sqrt{C_{\mathbf{w}}} > 0.9 \text{ TeV}$.
- We do not include operators that modify the Wud vertex since the current measurements of the hadronic width of the W are precise enough to ensure that such effects, if present, would be unobservable in the thj final state we consider, given the expected precision to which this reaction will be measured. We also ignored all flavor-changing operators and neglected all Yukawa-type interactions but those of the top quark.
- The term $\propto C_{\mathbf{h}}$ requires a (finite) wave-function renormalization of the Higgs field, $h \rightarrow (1 + C_{\mathbf{h}}\mathbf{v}^2/\Lambda^2)h$, under which all Higgs couplings are modified by the same factor [17]. This operator is generated at tree level by the exchange of either a heavy scalar neutral isosinglet or a scalar isotriplet. For simplicity, in the following we will ignore this operator; our main goal is to show that the introduction of operators other than $\mathcal{O}_{t\phi}$ (as required in an unbiased application of the EFT formalism) can significantly modify the limits on $\kappa_{\mathbf{t}}$, and for this it is sufficient to include $C_{4\mathbf{f}}$ and $C_{\mathbf{w}}$ (though, as we will show, the effects of the latter are small). Thus in the discussion below we assume $C_{\mathbf{h}} = 0$ for simplicity.

The NP effects we consider modify the tth and Wtb vertices in Fig. 1 and generate the additional graphs in Fig. 2. We assume $\mathcal{O}(1)$ values for the Wilson coefficients and absorb $|C_{\mathbf{w}}|$ in the definition of Λ (that is, we define the scale of NP of that the coefficient of $\mathcal{O}_{\phi q}^{(3)}$ is $\pm 1/\Lambda^2$ so that our model parameters are

$$\text{NP parameters: } \{C_{4\mathbf{f}}, C_{\mathbf{w}} = \pm 1, \kappa_{\mathbf{t}}, \Lambda\}, \quad (2.4)$$

where we use $\kappa_{\mathbf{t}}$ instead of $C_{\mathbf{t}}$ to allow easier comparison with the existing literature.

It is one of the goals of the present investigation to determine the extent to which the presence of non vanishing values of $C_{4\mathbf{f}, \mathbf{w}}$ affects the determination of $\kappa_{\mathbf{t}}$.

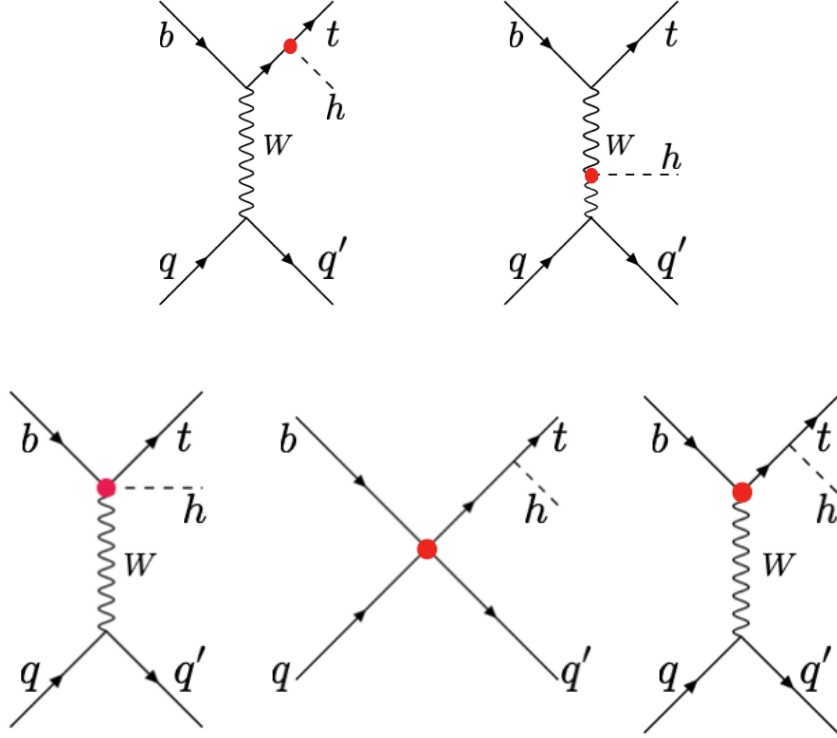


Figure 2. NP-induced vertices (shown by red blob) contributing to single-top production in association with a Higgs at the LHC.

2.1 Constraints on EFT Operator coefficients

There are several existing limits on the Wilson coefficients we consider. It is worth noting, however, that these may be conservative as they are often derived by assuming that a restricted number of effective operators are present.

- CMS [18] obtains the following exclusion limit using data from the 7 and 8 TeV LHC:

$$\frac{v^2}{\Lambda^2} |C_w| < 0.03 \quad \Rightarrow \quad \Lambda > 1.4 \text{ TeV} \quad (C_w = \mathcal{O}(1)). \quad (2.5)$$

that is comparable to the errors in $|V_{tb}|$ from CMS for the 13 TeV LHC [19]. This limit is obtained assuming the presence only of an EFT correction to the Wtb vertex, and will be degraded if the effects of other operators are included.

- The low energy constraints from B physics [20] give

$$-0.10 < \frac{v^2}{\Lambda^2} C_w < 0.15 \quad \Rightarrow \quad \Lambda > 780 - 640 \text{ GeV} \quad (C_w = \mathcal{O}(1)). \quad (2.6)$$

- The $t \rightarrow bud$ width receives a contribution from $\mathcal{O}_{qq}^{(3)}$ and $\mathcal{O}_{\phi q}^{(3)}$:

$$\Gamma(t \rightarrow bud) = \frac{m_t g^4 I_1}{2(8\pi)^3} \left[V_{tb}^2 + 2b_r + 2a_r \frac{I_2}{I_1} - 2\gamma a_i \right] + \mathcal{O}(1/\Lambda^4), \quad (2.7)$$

where g is the $SU(2)_L$ gauge coupling, $\gamma = \Gamma_{\mathbf{w}}/m_{\mathbf{w}} \simeq 0.026$, $r = m_{\mathbf{w}}/m_{\mathbf{t}} \simeq 0.46$,

$$a_{\mathbf{r}} + ia_{\mathbf{i}} = \frac{2v^2}{\Lambda^2} C_{4\mathbf{f}}; \quad b_{\mathbf{r}} = \frac{2v^2}{\Lambda^2} \mathbf{Re} C_{\mathbf{w}}; \quad (2.8)$$

and ⁶

$$I_1 = \frac{1}{\gamma r^2} \left\{ \pi + \arctan \left[\frac{\gamma}{(1 + \gamma^2)r^2 - 1} \right] \right\} \simeq 553.6, \\ I_2 = \frac{1}{2r^2} \ln \left[\frac{(1 - 1/r^2)^2 + \gamma^2}{1 + \gamma^2} \right] \simeq 5.9. \quad (2.9)$$

The sensitivity to $a_{\mathbf{i}}$ is much diminished because it appears multiplied by γ , the sensitivity to $a_{\mathbf{r}}$ is also small because $I_1 \gg I_2$ (I_1 gives the leading $\propto 1/\gamma$ contribution in the limit $\gamma \rightarrow 0$). The 3σ error in the width is about 40%; applying this to each coefficient separately ⁷

$$|a_{\mathbf{i}}| < 7, \quad |a_{\mathbf{r}}| < 19, \quad |b_{\mathbf{r}}| < 0.2. \quad (2.10)$$

For $\mathcal{O}(1)$ coefficients this gives $\Lambda > 130$ GeV, 80 GeV, 780 GeV respectively.

- Higgs production cross-section via gluon fusion is sensitive to $C_{\mathbf{t}}$ and $C_{\mathbf{h}}$. The contribution from these effective operators gives [17]

$$\sigma_{gg \rightarrow \mathbf{h}} = \left(1 + \frac{\sqrt{2}v^3}{m_{\mathbf{t}} \Lambda^2} C_{\mathbf{t}} + \frac{2v^2}{\Lambda^2} C_{\mathbf{h}} \right) \sigma_{gg \rightarrow \mathbf{h}}^{(\text{SM})}, \quad (2.11)$$

where we assumed $C_{\mathbf{t}}$ real. The 3σ error on this cross-section is $\sim 20\%$ that translates into $\Lambda > 780$ GeV for $C_{\mathbf{t},\mathbf{h}} = \mathcal{O}(1)$ (and no cancellations).

- The coefficient $C_{\mathbf{h}}$ is also constrained by the $h \rightarrow ZZ^*$, WW^* decay widths [17]:

$$\frac{\Gamma(h \rightarrow ZZ^*)}{\Gamma_{\text{SM}}(h \rightarrow ZZ^*)} = \frac{\Gamma(h \rightarrow WW^*)}{\Gamma_{\text{SM}}(h \rightarrow WW^*)} = 1 + \frac{v^2}{\Lambda^2} C_{\mathbf{h}}. \quad (2.12)$$

The ZZ^* and WW^* widths have 3σ uncertainties of $\sim 25\%$ and $\sim 30\%$, respectively, which give $\Lambda > 500$ GeV, 450 GeV, when $|C_{\mathbf{h}}| \sim 1$.

- The TopFitter collaboration [21] reports the individual limits,

$$\Lambda > 960 \text{ GeV} \quad \text{when } |C_{4\mathbf{f}}| = 1 \\ \Lambda > 720 \text{ GeV} \quad \text{when } |C_{\mathbf{w}}| = 1 \quad (2.13)$$

at 95% CL (the marginalized limits are 800 GeV and 510 GeV, respectively); these are comparable to the above constraints.

⁶To $\mathcal{O}(1/\Lambda^2)$ the width does not depend on $\mathbf{Im} C_{\mathbf{w}}$.

⁷These limits do not hold if there are cancellations.

2.2 Validity of the EFT approximation

Under the current assumptions of a weakly-coupled and decoupling heavy physics, the fundamental limitation in using an EFT approximation is the condition that the typical energy is smaller than Λ , for otherwise, the experiment(s) under consideration would have sufficient energy to directly create the new heavy particles. However, in order to impose this condition, the definition of ‘typical’ energy requires some clarification.

Consider, for example, the 4-fermion vertex $(\bar{d}_L \gamma_\mu u_L)(\bar{t}_L \gamma^\mu b_L)$ derived from the 4-fermion operators in eq. (2.1). As noted in that section, there are other operators that generate the same vertex, but these are Fierz-equivalent to those in eq. (2.1); explicitly

$$\begin{aligned}\mathcal{O}_{qq}^{(8;1)} &= (\bar{q}_t \gamma_\mu T^A q_u)(\bar{q}_u \gamma^\mu T^A q_t) = \frac{2}{3} \mathcal{O}_{qq;1}^{(1)} - \mathcal{O}_{qq;1}^{(3)} - \mathcal{O}', \\ \mathcal{O}_{qq}^{(8;3)} &= (\bar{q}_t \gamma_\mu T^A \tau^I q_u)(\bar{q}_u \gamma^\mu T^A \tau^I q_t) = \frac{2}{3} \mathcal{O}_{qq;2}^{(3)} + \mathcal{O}_{qq;1}^{(3)} - \mathcal{O}',\end{aligned}\quad (2.14)$$

where $\mathcal{O}' = (\bar{q}_t \gamma_\mu q_t)(\bar{q}_u \gamma^\mu q_u)$.

It is worth noting that neither \mathcal{O}' nor the two related operators $(\bar{q}_t \gamma_\mu T^A \tau^I q_t)(\bar{q}_u \gamma^\mu T^A \tau^I q_u)$ and $(\bar{q}_t \gamma_\mu T^A \tau^I q_t)(\bar{q}_u \gamma^\mu T^A \tau^I q_u)$ produce a vertex $(\bar{d}_L \gamma_\mu u_L)(\bar{t}_L \gamma^\mu b_L)$, and do not interfere with the SM contribution; they are not discussed further for this reason.

From these considerations we can immediately determine the type of heavy physics that can generate the vertex $(\bar{d}_L \gamma_\mu u_L)(\bar{t}_L \gamma^\mu b_L)$ at tree level:

vector	$SU(2)$	$SU(3)$	couplings	operator generated	reference
$X^{(1;1)}$	1	1	$\bar{q}_u \gamma^\mu q_t$	$\mathcal{O}_{qq}^{(1)}$	eq. (2.1)
$Y_1^{(3;1)}$	3	1	$\bar{q}_a \gamma^\mu \tau^I q_a, \ (a = u, t)$	$\mathcal{O}_{qq;1}^{(3)}$	eq. (2.1)
$Y_2^{(3;1)}$	3	1	$\bar{q}_u \gamma^\mu \tau^I q_t$	$\mathcal{O}_{qq;2}^{(3)}$	eq. (2.1)
$Y_3^{(3;8)}$	3	8	$\bar{q}_u \gamma^\mu \tau^I T^A q_t$	$\mathcal{O}_{qq}^{(8;3)}$	eq. (2.14)
$V^{(1;8)}$	1	8	$\bar{q}_u \gamma^\mu T^A q_t$	$\mathcal{O}_{qq}^{(8;1)}$	eq. (2.14)

(superscripts in the vector fields correspond to their $SU(2) \times SU(3)$ transformation properties). Consider now the reactions⁸ $bq \rightarrow tq'$ and $qq' \rightarrow t\bar{b}$, where q, q' are light quarks or antiquarks, then the above heavy vectors contribute in either s or t channels as listed below:

	$X^{(1;1)}$	$V^{(1;8)}$	$Y_1^{(3;1)}$	$Y_2^{(3;1)}$	$Y_3^{(3;8)}$
$bq \rightarrow tq'$	s	s	t	s	s
$qq' \rightarrow t\bar{b}$	t	t	s	t	t

For the process $qq' \rightarrow t\bar{b}$ with a quark-level CM energy $E_{\text{CM}}(t\bar{b})$ the EFT will be valid provided the mass of the vector boson obeys $m(Y_1) > E_{\text{CM}}(t\bar{b})$; the corresponding constraints for the other vector boson masses will be much weaker because the typical values of the t-channel momentum transfer are much smaller than $E_{\text{CM}}(t\bar{b})$. In contrast, for the process

⁸ $t\bar{b}$ can contribute to the final state of interest when b is mistagged as a forward light jet.

$bq \rightarrow tq'$ we must have $m(X)$, $m(V)$, $m(Y_2)$ and $m(Y_3)$ all larger than $E_{\text{CM}}(tq')$ (the CM energy for that reaction) for the EFT approximation to be valid. Therefore the potential NP contribution to tq' production comes from $Y_1^{(3;1)}$, which has subdued contribution to $t\bar{b}$ production, and is neglected. Experimental limits (see [22] and references therein) requires $m(Y_1)$ to be above several TeV⁹. The corresponding analysis for the reaction at hand is discussed in section 3.2 below.

3 Limits using current LHC data

The essence of studying EFT operator contributions to the SM processes at collider is dominantly two fold: (i) estimating the limit on NP parameters for current CM energy and luminosity, and (ii) evaluating the contribution of EFT operators to future sensitivities to find out the discovery limit after a careful background estimation/reduction. The methodology for both are similar; however in the first case, one needs to adhere to the event selection strategy used in the existing experimental analysis as closely as possible. We elaborate upon the first part in this section, while the discovery potential in future luminosities is discussed in the next section.

3.1 Model implementation and production cross-section

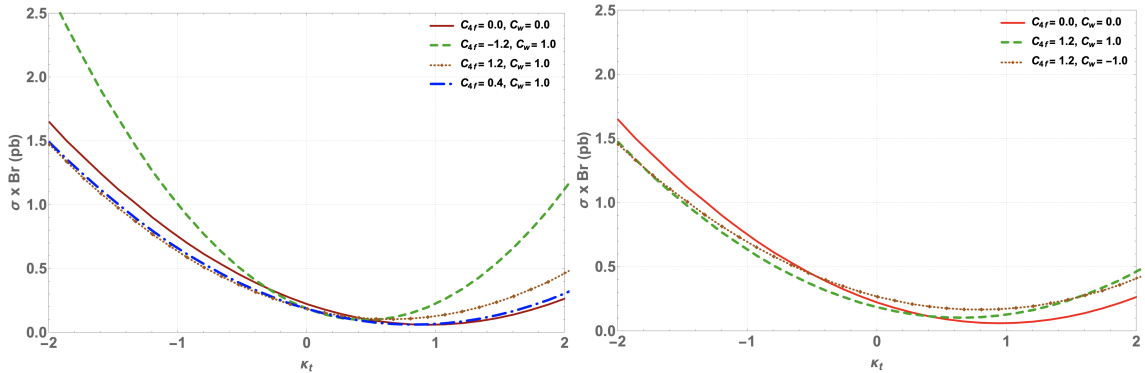


Figure 3. Dependence of thj production cross-section on κ_t in presence of EFT operators when $\Lambda = 1$ TeV. Left: $C_w = 1$ and several values of C_{4f} chosen as $\{-1.2, +1.2, 0.4\}$; Right: $C_{4f} = 1$ and C_w are chosen as $\{-1, 1\}$. We also compare them with the case where $C_{4f} = C_w = 0$, with variable κ_t (shown by the red thick line). All cross-sections are evaluated at the LHC with $\sqrt{s} = 13$ TeV. The branching ratio (Br) of Higgs includes $h \rightarrow WW^*, ZZ^*, \gamma\gamma, b\bar{b}, \tau\bar{\tau}$.

We first estimate the contribution of EFT operators to thj production following the operators listed in Eq. (2.2) and Feynman graphs as in fig. 2. The methodology is simple. We insert the effective Lagrangian Eq. (2.2) in the `FeynRules` [23] code and create files

⁹We may also note here that in SM $qq' \rightarrow t\bar{b}$ production is small, for example, $th\bar{b}$ production cross-section is 2.26 fb at the LHC with $\sqrt{s} = 14$ TeV, significantly below than thj production cross-section.

compatible for event simulation in MadGraph5_aMC@NLO [8]. We generate events including SM and EFT contributions together, and plot the cross-section as a function of κ_t (which is equivalent to C_t) at $\sqrt{s}=13$ TeV (we use this notation to simplify the comparison of the outcome with CMS results in [7]). In fig. 3, we show the variation of thj cross-section times the branching ratio (Br) of Higgs $\rightarrow WW^*, ZZ^*, \gamma\gamma, b\bar{b}, \tau\bar{\tau}$, in presence of EFT operators assuming the NP scale $\Lambda = 1$ TeV. In the left plot we have kept fixed $C_w = 1$ and chosen different C_{4f} as $\{-1.2, +1.2, 0.4\}$ (cf. the figure inset). On the right panel, a similar calculation is done fixing $C_{4f} = 1$ and varying C_w for two values $\{-1, 1\}$. All these points are compared to the case where both $C_w, C_{4f} = 0$, keeping κ_t as variable on which the cross-section depends. In both the cases, we see that with larger $|\kappa_t|$, the cross-section grows, as expected. Importantly, it is worth noting that for $C_{4f} > 0$, the thj cross-section is smaller than SM only contribution for $\kappa_t < 0$. Similarly, for $C_{4f} < 0$, the cross-section is larger than the SM only contribution for both positive and negative κ_t . We also can see that the contribution of C_w is much milder than that of C_{4f} . It is worth reminding here that in the recent analysis for single top production at LHC [13], the contribution from C_{4f} has completely been ignored, which clearly plays a more dominating role than other operators.

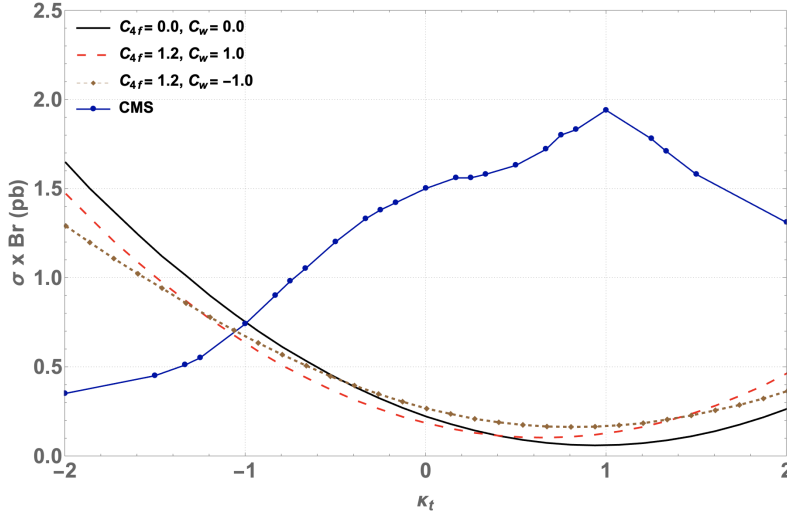


Figure 4. thj cross-section (σ) times branching ratio (Br) of Higgs $\rightarrow WW^*, ZZ^*, \gamma\gamma, b\bar{b}, \tau\bar{\tau}$, for several benchmark points of the model (see figure legend), including that of $C_{4f}, C_w = 0$ and variable κ_t (black thick line), confronted with CMS observed data (dotted solid line) [7]. Note that the data (dotted solid line) meets the SM cross-section (black solid line) at $\kappa_t = -0.9$.

The comparison to the recent most LHC data [7] is shown in fig. 4. In this figure, along the y-axis here, we plot thj production cross-section times the branching ratio of Higgs to all final states except for the gluon pair ($h \rightarrow WW^*, ZZ^*, \gamma\gamma, b\bar{b}, \tau\bar{\tau}$), in accordance to the CMS analysis [7]. The dot-thick line in blue indicates the bound obtained from the LHC data with $\sqrt{s} = 13$ TeV and integrated luminosity $\mathcal{L} = 35.9 \text{ fb}^{-1}$ as a function of

κ_t . For model example, we chose combinations of Wilson coefficients that provide good illustrations of the important operators other than $\mathcal{O}_{t\phi}$ can have (see figure inset legends); for example choosing $C_w = 1$, $C_{4f} = 1.2$ minimizes the cross-section when $\kappa_t = -1$, while $C_w = -1.0$, $C_{4f} = 0.8$ corresponds to maximum cross-section when $\kappa_t = +1$, when the Wilson coefficients are varied within $\{-1.2, +1.2\}$. The plot shows that the presence of $\mathcal{O}_{qq,\phi q}^{(3)}$ can alter the limits $\kappa_t < -0.9$ obtained [7] in absence of these operators. We can also see that for $C_w = C_{4f} = 0$ and $\kappa_t = 1$, we recover the SM cross-section times branching ratio ~ 70 fb.

There are a few more comments in order. First, although we clearly see that $C_{h,4f,w} \neq 0$ changes the experimental limit as in fig. 4, one needs to set a criteria for obtaining the bound on the EFT parameters from the existing data. This is elaborated on in the next subsection. Second, the presence of these EFT operators provides a significant departure from the signal events compared to the SM, so judicious cuts on kinematic variables or BDT analysis paves the way for discovery potential. Lastly, we note that these operators contribute to other processes like top decay, etc.; while choosing the values of the Wilson coefficients and NP scale, we abide by such limits.

Before proceeding further we note here that EFT approximation at collider is valid when the NP scale is larger than the CM energy of the reaction,

$$\text{Validity of EFT at LHC : } \Lambda > \sqrt{\hat{s}}. \quad (3.1)$$

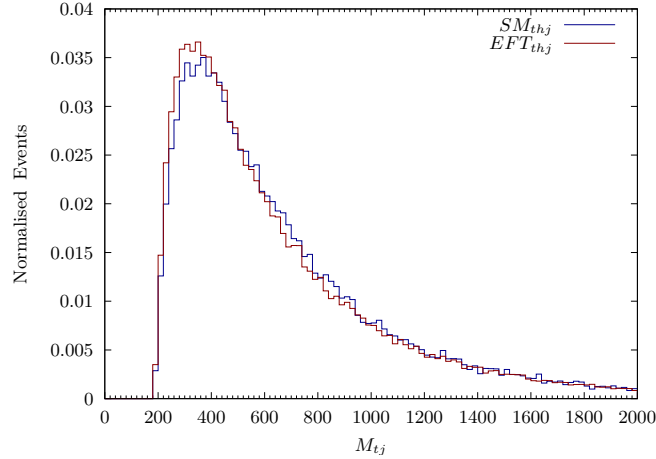


Figure 5. Invariant mass (M_{tj}) distribution for the thj signal production with EFT contributions assuming $\Lambda = 1$ TeV and all the parameters $\{C_{4f}, C_w, \kappa_t\}$ set to one, at LHC with $\sqrt{s} = 13$ TeV. We also depict the distribution with SM contribution only. The production cross-section is normalized to one.

However, ensuring this limit is difficult at LHC, due to the unknown and variable subprocess CM energy \hat{s} . One can however have an estimate of the partonic CM energy

by constructing the invariant mass of the final state particles,

$$M_{inv}^2 = \left(\sum_i p_i \right)^2 ; \quad (3.2)$$

where p_i represents four-momenta and i runs over all or a subset of the visible set of detectable final state particles. The appropriate choice of invariant mass depends on whether it is a $s/u/t$ channel reaction, thus segregating different types of NP contributions, see for example, [24]. Now, if the M_{inv} distribution peaks at a smaller value than the chosen NP scale (Λ), then the bulk of the events are produced with CM energy smaller than Λ , validating the EFT nature of the interaction. In fig. 5, we plot invariant mass distribution M_{tj} for SM plus EFT contribution assuming $\Lambda = 1$ TeV, with $\{C_{4f}, C_w, \kappa_t\} = 1$ at the LHC with $\sqrt{s} = 13$ TeV, to show that the peak arises ~ 500 GeV $< \Lambda$, thus validating of the EFT nature of the interaction.

3.2 Event Analysis and simulation techniques

We generate all the event samples using `MadGraph5_aMC@NLO` [8] at parton-level in leading order (LO) and a dedicated universal FeynRules output (UFO) model for the EFT framework was produced using `FeynRules`. We have used the 5-flavor scheme [25] of parton distribution function with the NNPDF30LO PDF set [26]. The default `MadGraph5_aMC@NLO` LO dynamical scale was used, which is the transverse mass calculated by a k_T -clustering of the final-state partons. Then we interface the events with the Pythia 8 [27] parton shower. Events of different jet-multiplicities were matched using the MLM scheme [28] with the default `MadGraph5_aMC@NLO` parameters and all samples were processed through `Delphes 3` [29], which simulates the detector effects, applies simplified reconstruction algorithms and was used for the reconstruction of electrons, muons, and hadronic jets.

For the leptons ℓ (electrons and muons) the reconstruction was based on transverse momentum (p_T)-and pseudo-rapidity (η)-dependent efficiency parametrization. Isolation of a lepton from other energy-flow objects was applied in a cone of $\Delta R = \sqrt{\Delta\eta^2 + \Delta\phi^2} = 0.4$ with a minimum $(p_T)_\ell > 25$ GeV. We reconstruct the jets using the anti- K_T clustering algorithm [30] with a radius parameter of $\Delta R = 0.4$ implemented in `FastJet` [31, 32]. The identification of b -tagged jets was done by applying a p_T -dependent weight based on the jet's associated flavor, and the MV2c20 tagging algorithm [33] in the 70% working point.

thj production within SM and beyond (including EFT operators) leads to different possible final states following subsequent decay modes of the top quark and the Higgs boson. Each different final state faces different non-interfering SM background contributions, thereby altering the signal extraction strategy and event simulation. We focus here on the same sign dilepton (SSD) signal with both leptons having positive or negative charges that may arise with different flavours ($\ell = e, \mu$) associated with one forward jet¹⁰ and two other jets (j), resulting from the following decay chain:

$$\text{Signal (SSD)} : pp \rightarrow thj, \quad t \rightarrow bW^+ \rightarrow b\ell^+\nu, \quad h \rightarrow W^-W^{+*} \rightarrow (jj)(\ell^+\nu).$$

¹⁰By forward jet, we refer to the jet having maximum pseudorapidity in an event.

The dominant SM background arises from $t\bar{t}W$, which also contributes to the same final state signal. Other processes that contribute as non-interfering background are $t\bar{t}Z$, WZ and $t\bar{t}$. The contribution from $t\bar{t}$ to the same sign dilepton signal arises due to the leptons coming out of bottom meson decay. Apart, $t\bar{t}h$ can also contribute to the signal, which is sensitive to the Wilson coefficients, κ_t in particular. As we are not tagging the top quarks in the final state, $t\bar{t}h$ can be considered as part of the signal in principle¹¹. However, as a conservative estimate, we do not consider this process while scanning the parameter space for the signal significance, although the contribution at the selected benchmark points are estimated. Adhering to the CMS analysis [7], we adopt the basic cuts as follows:

- Demanding exactly two same sign dilepton (ℓ) with the combination $\mu^\pm\mu^\pm$ or $e^\pm\mu^\pm$, following the reconstruction methodology as described above.
- $(p_T)_\ell > 25/15$ GeV and no loose lepton with invariant mass $m_{\ell\ell} < 12$ GeV.
- Event should comprise of one or more b -tagged jet with $p_T > 25$ GeV within $|\eta| < 2.4$.
- One or more untagged jets with $p_T > 25$ GeV within $|\eta| < 2.4$, and $p_T > 40$ GeV for $|\eta| > 2.4$ following the jet reconstruction technique.

We further define,

$$\epsilon_{cut} = \frac{\sigma^{\text{SSD}}}{\sigma^{\text{prod}}}, \quad (3.3)$$

where σ^{SSD} indicate final state SSD signal cross-section surviving after taking into account appropriate branching ratios and basic cuts and σ^{prod} represents thj production cross-section.

As the observed number of events at the LHC after the final BDT analysis is not available, it is important to ask how to set a limit on our EFT parameter space $\{C_{4f}, C_w, \kappa_t, \Lambda\}$ from the observed data. Following the CMS observation [7], we simulate thj production for SM processes *without* EFT contribution for $\kappa_t = -0.9$ to produce same sign dilepton (SSD) events using the basic cuts at $C_{4f} \sqrt{s} = 13$ TeV and integrated luminosity $\mathcal{L} = 35.9$ fb⁻¹. Thus obtained number of events (N_0) is used to set the limit on the EFT parameters,

$$N_0 = (\sigma^{thj})_{SM}|_{\kappa_t=-0.9} \times \epsilon_{cut} (0.15\%) \times \mathcal{L} (35.9 \text{ fb}^{-1}) = 37. \quad (3.4)$$

We note here that N_0 is specific to the SSD channel produced from thj , which uses the CMS exclusion limit of κ_t inferred from all possible Higgs decay modes excepting for gluon gluon. Also there is a certain element of uncertainty in the estimation of this number due to the model dependence of the ϵ_{cut} , which is rather small given the range of Wilson coefficients scanned in this analysis, as explained later on.

We next choose a few representative benchmark points with EFT contributions (BP0-BP4) and note the production cross-section (σ_p), number of events after the basic cuts

¹¹The CMS analysis [7] also has considered $t\bar{t}h$ as part of the signal.

Benchmarks	$\{\kappa_t, C_{4f}, C_w\}$	σ_{prod} (fb)	N_{bc}	ϵ_{cut}
SM thj	$\{1.0, 0, 0\}$	71.0	3.9	0.0015
BP0	$\{-1.0, 0, 0\}$	888.81	47.61	0.0017
BP1	$\{-1.0, 1.2, 1.0\}$	773.05	39.0	0.00172
BP2	$\{-0.5, 1.2, -1.0\}$	522.29	26.46	0.001675
BP3	$\{0.5, 0.4, 1.0\}$	95.06	4.38	0.00152
BP4	$\{1.0, 0.8, -1.0\}$	134.05	6.01	0.0014
$t\bar{t}W$	$\{1.0, 0, 0\}$	566	164.14	0.013
$t\bar{t}Z$	$\{1.0, 0, 0\}$	863	78.39	0.013
$t\bar{t}$	$\{1.0, 0, 0\}$	839×10^3	198.17	1.6×10^{-5}

Table 1. Production cross-section (σ_p), number of SSD signal events after the basic cuts (N_{bc}) and cut efficiency (ϵ_{cut}) in SM, together with EFT contributions for benchmark points BP0-BP4 at the LHC with $\sqrt{s} = 13$ TeV and integrated luminosity $\mathcal{L} = 35.9 \text{ fb}^{-1}$. SM background ($t\bar{t}W$, $t\bar{t}Z$, $t\bar{t}$) contributions are also noted after including appropriate K factors (see text). All the cross-sections for the signal benchmark points are obtained after multiplying by the K factor 1.187.

Model	Contribution with $C_{4f} = C_w = 0$	Interference contribution	Pure EFT contribution
BP1	748.6	$-221.38 (1 \text{ TeV}/\Lambda)^2$	$123.78 (1 \text{ TeV}/\Lambda)^4$
BP2	435.0	$-24.43 (1 \text{ TeV}/\Lambda)^2$	$28.79 (1 \text{ TeV}/\Lambda)^4$
BP3	91.52	$-21.67 (1 \text{ TeV}/\Lambda)^2$	$9.38 (1 \text{ TeV}/\Lambda)^4$
BP4	59.8	$-18.32 (1 \text{ TeV}/\Lambda)^2$	$71.42 (1 \text{ TeV}/\Lambda)^4$

Table 2. Contribution to thj production cross-section (in fb) from the dimension six EFT operators considered in Eq. (2.1), divided into interference term ($\sim 1/\Lambda^2$) and pure NP contribution ($\sim 1/\Lambda^4$) with Λ in TeV for the benchmark points as in Table 1. One can obtain the cross-sections as in Table 1 using $\Lambda = 1$ TeV after multiplying by the K factor 1.187.

(N_{bc}) and cut efficiency ϵ_{cut} at the LHC with $\sqrt{s} = 13$ TeV and $\mathcal{L} = 35.9 \text{ fb}^{-1}$ in Table 1. SM thj production, NLO contributions from the dominant SM backgrounds $t\bar{t}W$, $t\bar{t}Z$, along with $t\bar{t}$ are all pointed out. The K -factors used for $t\bar{t}W(t\bar{t}Z)$ is 1.78 (1.51) [34], SM thj is 1.18 [7].

The benchmark points are chosen with different values of κ_t with a combination of $\{C_{4f}, C_w\}$ so that they capture some interesting physics, where the Wilson coefficients vary maximally within $\{-1.2, 1.2\}$. For example, BP1: $\{\kappa_t, C_{4f}, C_w\} = \{-1.0, 1.2, 1.0\}$ *minimizes* the thj cross-section at $\kappa_t = -1$ and BP4: $\{1.0, 0.8, -1.0\}$ *maximizes* the cross-section at $\kappa_t = +1$, within the range in which the Wilson coefficients have been varied.

BP2: $\{-0.5, 1.2, -1.0\}$ and BP3: $\{0.5, 0.4, 1.0\}$ are chosen with intermediate κ_t ¹². BP0 refers to a point with $\kappa_t = -1$ with other NP couplings set to zero; when compared to BP1, this shows how the choices of $\{C_{4f}, C_w\}$ can alter the cross-section for a given κ_t . Also note that BP1 produces events very close to the exclusion limit and kept as a reference due to uncertainties in pdfs, choice of renormalization, and factorization scales at the hadron collider. In Table 2, the relative contribution of the interference term and pure EFT contribution to the thj production cross-section at the benchmark points are shown as a function of Λ (TeV). We see that when the pure κ_t dependent contribution is small (this can happen when κ_t takes positive values or small negative values) and/or C_{4f} is large, pure EFT contribution $\sim 1/\Lambda^4$ can be significant. We would also like to mention that the benchmark points presented here are just indicative of different features of the EFT contribution to thj signal, while a detailed scan in the κ_t, C_{4f} plane is provided both in the current limit and for future sensitivities of LHC for different choices of C_w .

Further, we note the presence of almost uniform ϵ_{cut} for all the benchmark points, Table 1 suggests that it varies within 0.0014-0.0017. A constant or slowly varying ϵ_{cut} basically indicates that the branching ratios and cut sensitivity are almost uniform for different choices of EFT benchmark points. Therefore, ϵ_{cut} can be used effectively to multiply with the **MadGraph** level production cross-section to match signal-level SSD events. This methodology is used to put a bound on the cross-section times branching ratio in the EFT $\kappa_t - C_{4f}$ parameter space as shown in fig. 6. Following the fact that C_w affects the cross-section mildly, we have kept $C_w = 1$ (left), -1 (right); the events are simulated at 35.9 fb^{-1} luminosity at $\sqrt{s} = 13 \text{ TeV}$. In this figure the cross-section times branching ratio to obtain SSD signal is shown by the colour gradient, where the darker shades indicate smaller number of signal events and lighter shades indicate a larger signal cross-section. It is easy to appreciate that larger κ_t, C_{4f} provide larger signal cross-section. The bound¹³ obtained from CMS as described in Eq. (3.4) is shown by the white lines. The CMS bound excludes thj cross-section times branching ratio $\gtrsim 0.3 \text{ pb}$. This is equivalent to large values of $|\kappa_t|$, which is mildly dependent on C_{4f} for $\kappa_t < 0$. The limit $\kappa_t < -0.9$ is obtained for $C_{4f} = 0$, in agreement with the CMS limit. The limit on κ_t gets tighter for $C_{4f} < 0$ and relaxed for $C_{4f} > 0$, allowing upto $\kappa_t \sim -1.0$ (within $-2 < C_{4f} < 2$). Lastly we note that for $\kappa_t > 0$, the cross-section as well as the CMS limit depends on C_{4f} very crucially. For $C_{4f} = 0$, there is no upper bound on κ_t (within the range it has been varied) also in agreement with the CMS analysis. We also see that there is an asymmetry in the dependence on C_{4f} for large values of C_{4f} with $\kappa_t > 0$, which indicates to a non-negligible contribution proportional to $\sim C_{4f}^2$ beyond the interference term $\sim C_{4f}\kappa_t$, as observed from the selected benchmark points in Table 2.

We further note that the operators with Wilson coefficient C_w contributes to tbW vertex and therefore to $t\bar{t}W$ background. However the contribution of the relevant t-channel graph of $t\bar{t}W$ production is very little, therefore the change is of the order of 0.1% of the cross-section and can be safely ignored. On the other hand, C_{4f} coupling can

¹²For negative (positive) κ_t , similar choice of $\{C_{4f}, C_w\}$ minimizes/maximizes the cross-section.

¹³There exists almost 13% uncertainty in the estimation of N_0 from Eq. (3.4), owing to the mild variation of ϵ_{cut} .

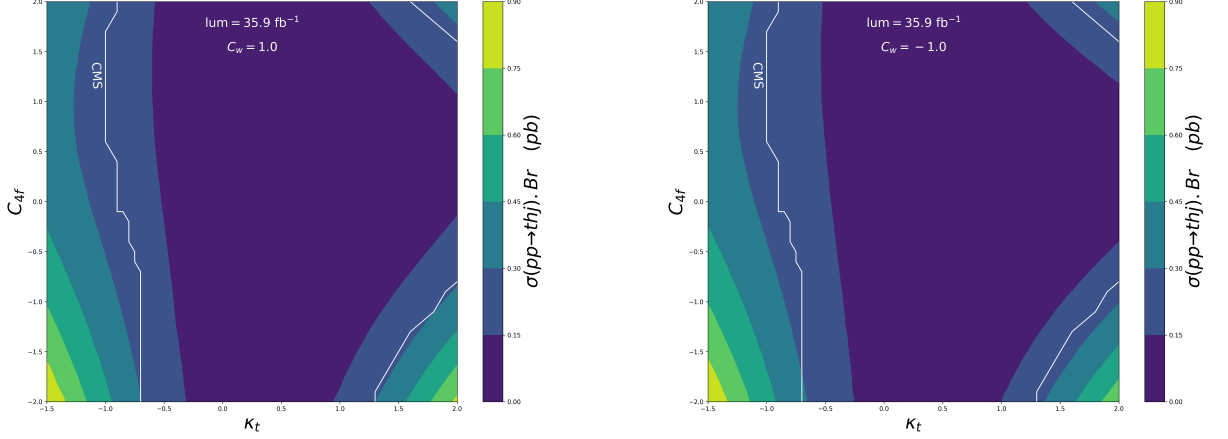


Figure 6. Scan for thj production cross-section times branching ratio (in pb) to get SSD signal at LHC in $C_{4f} - \kappa_t$ plane for $C_w = 1$ (left), -1 (right) at 35.9 fb^{-1} luminosity for $\sqrt{s} = 13 \text{ TeV}$. Signal cross-section is shown by colour gradient, where lighter shades represent larger cross-section. The bound from observed data in CMS (see Eq. 3.4) is shown by white lines and the region outside the boundary is excluded by the bound.

contribute to $t\bar{b}$ production via four fermi interaction (see the Feynman graph in the middle of the lower panel of Fig. 2), upon a W radiation, which can contribute non-negligibly $\sim 10\%$ to $t\bar{t}W$ production when no NP is assumed. However, as argued in section 2.2, the NP that contributes substantially to thj signal ($Y_1^{(3;1)}$, see Eq. (2.15) and Eq. (2.16)), will contribute to $t\bar{t}W$ via s channel mediation, and will be suppressed. On the other hand, C_{4f} contribution to $t\bar{t}Z$ via $Y_1^{(3;1)}$ is non-negligible, but are suppressed by b parton distribution functions in the initial state. Other NP effects like $Y_1^{(3;2)}$ are again s -channel suppressed and produce mild effects $\sim 1\%$. Note however, that in estimating above limits, we are talking only about those NP effects which contribute to the ‘chosen’ signal significantly. There are dedicated analysis for $t\bar{t}Z, t\bar{t}\gamma, t\bar{t}h$ production in presence of non-negligible EFT contributions, see for example, [35]. Global fit of SMEFT operators in different channels has been considered in literature exhaustively [36], however a dedicated analysis including $tj, thj, t\bar{t}V, t\bar{t}\gamma, t\bar{t}h$ channels is yet to be done, but remains beyond the scope of the present draft.

4 Upcoming sensitivities at LHC

In this section, we refer to the sensitivity with full run-2 data set of LHC at $\sqrt{s} = 13 \text{ TeV}$. The discovery potential of the signal events depends on the efficiency of reducing the SM background contribution, retaining the signal to the extent possible. We observe some key distinctive features between the signal events (thj) and the SM background contributions

Signal : $pp \rightarrow thj$	SM background: $pp \rightarrow t\bar{t}W$
$t \rightarrow bW^+ \rightarrow b\ell^+\nu$, $h \rightarrow W^-W^{+*} \rightarrow (jj)(\ell^+\nu)$	$t\bar{t}W \rightarrow (bW^-)(bW^+)W \rightarrow (b\ell^-\nu)(bjj)(\ell^-\nu)$
One forward jet	No forward jet
b -jet multiplicity peaks near 1	b -jet multiplicity peaks near 2
No reconstructed top in bjj mode	One reconstructed top in bjj mode
$ \Delta\eta _{bj_F}$ peaks at large values	$ \Delta\eta _{bj_F}$ peaks at smaller values
$ \Delta\eta _{\ell j_F}$ peaks at large values	$ \Delta\eta _{\ell j_F}$ peaks at smaller values

Table 3. Key distinctive features in SSD events coming from thj signal and $t\bar{t}W$ SM background contributions. The distinctive features remain same for $t\bar{t}Z$ also.

($t\bar{t}W$) as summarized in Table 3. They include: (i) absence of a forward jet in SM ($t\bar{t}W$) background, (ii) b -jet multiplicity peaks at 1 for thj signal, whereas for background ($t\bar{t}W$) it peaks at 2 having two top quarks at the production level, (iii) pseudorapidity difference $\Delta\eta$ between the forward jet and b -jet ($|\Delta\eta|_{bj_F}$) is also expected to be different for signal and background, (iv) $|\Delta\eta|$ between b -jet and closest lepton ($|\Delta\eta|_{\ell j_F}$) can also provide a distinction between the signal and background.

We show the distributions of SSD events coming from SM thj production with $\kappa_t = 1.0$ (in blue shaded region) and SM background events coming from $t\bar{t}W$ in red hatched regions (all normalized to one) in fig. 7 for the key variables which have been identified to distinguish these two cases; namely, $|\eta|$ of the forward jet (top left), $(\Delta\eta)_{j_F b}$ with leading b jet (top right), $(\Delta\eta)_{j_F b}$ with sub leading b jet (bottom left) and $\Delta\eta_{\ell j_F}$ between forward jet and closest lepton (bottom right) at LHC with $\sqrt{s} = 13$ TeV. From these distributions, we clearly see that all of these variables can be used judiciously to tame the SM background contribution and elucidate the signal events, be it in a cut-based analysis or using machine learning techniques. In fig. 8, we show the same distributions for different benchmark points (BP1-BP4) without the SM background. We find that the signal distributions are not characteristically different for different choices of κ_t or C_{4f}, C_w . Therefore, uniform signal selection criteria can be used for all the allowed regions in the $\kappa_t - C_{4f}$ parameter space. Note here that the distributions are made with the number of events generated at $\mathcal{L} = 35.9 \text{ fb}^{-1}$, but normalized to one.

4.1 Cut-based analysis

We chose judicious cuts that distinguish the signal and background events effectively as mentioned in Table 4, which can also be appreciated from the distributions shown in fig. 7. The efficiency of these cuts to retain signal and eliminate SM background is shown in Table 5 via cut flow for all the benchmark points BP0-BP4. $t\bar{t}h$ cross-section at the benchmark points are shown separately in Table 6, where we have used the SM K -factor to normalise the cross-section for all the EFT benchmark points. The maximum $t\bar{t}h$ cross-section in the region of parameter space we are interested in is $\sim 567 \text{ fb}$ and the maximum

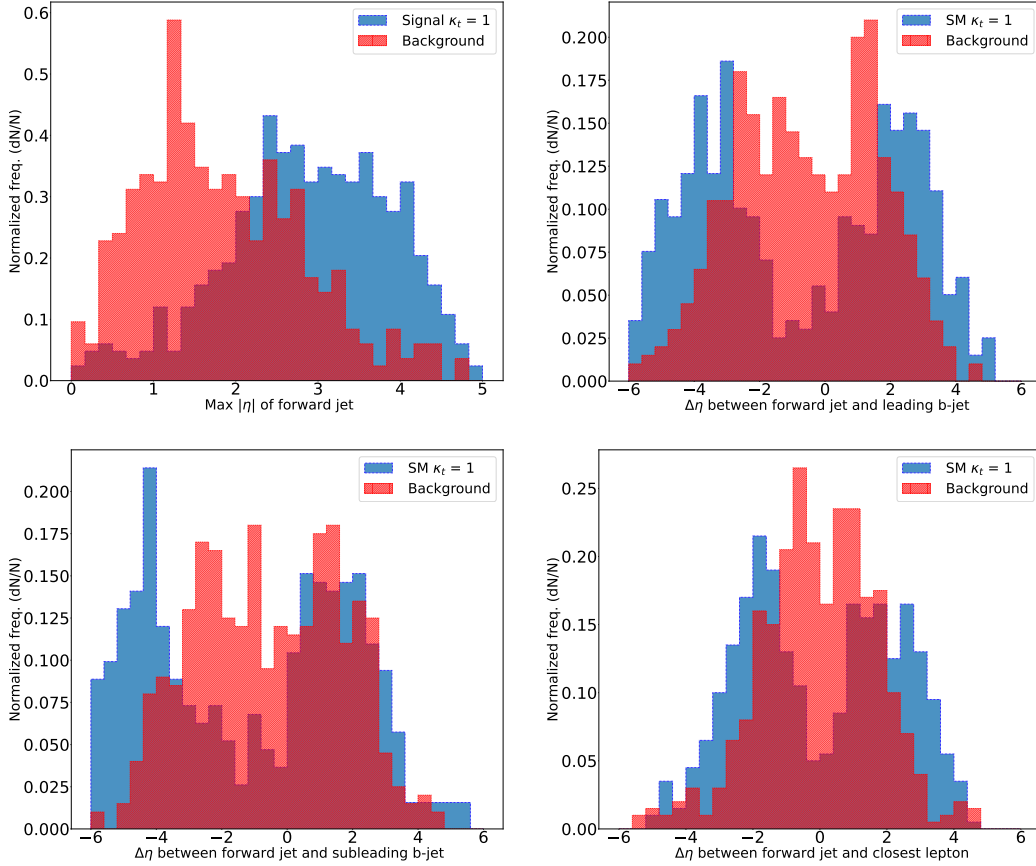


Figure 7. Distribution of SSD events coming from SM thj (with $\kappa_t = 1.0$ in blue shaded region) and SM background ($t\bar{t}W$) in red hatched region (all normalized to one) for $|\eta|$ of the forward jet (top left), $(\Delta\eta)_{j_F b}$ with leading b jet (top right), $(\Delta\eta)_{j_F b}$ with sub leading b jet (bottom left) and $(\Delta\eta)_{\ell j_F}$ (bottom right) between forward jet and closest lepton at LHC with $\sqrt{s} = 13$ TeV.

signal contribution after implementing the hard cuts is 13 -14 events. Evidently, if this process is included in the background, the estimated signal significance will drop by a few %. For instance, at BP2, the significance reduces to 2.07 from 2.19, whereas for BP3, the significance drops to 0.44 from 0.47 at $\sqrt{s} = 13$ TeV with 35.9 fb^{-1} luminosity. We also note that the $t\bar{t}$ contribution to the signal can be tamed down after imposing harder set of cuts for example, demanding only one b -tagged jet, higher jet rapidity cut like $|\eta|_{j_F} \geq 2.5$, and stronger lepton-jet isolation criteria, without much affecting the signal event rate. In the scans for signal significance, we omit $t\bar{t}$ contribution.

We also calculate the signal significance $z(z_1)$ defined by:

$$z_1 = \frac{S_1}{\sqrt{S+B}}, \quad z = \frac{S}{\sqrt{S+B}}, \quad S_1 = S - S'; \quad (4.1)$$

where S refers to the signal events including EFT, S' refers to signal contribution just

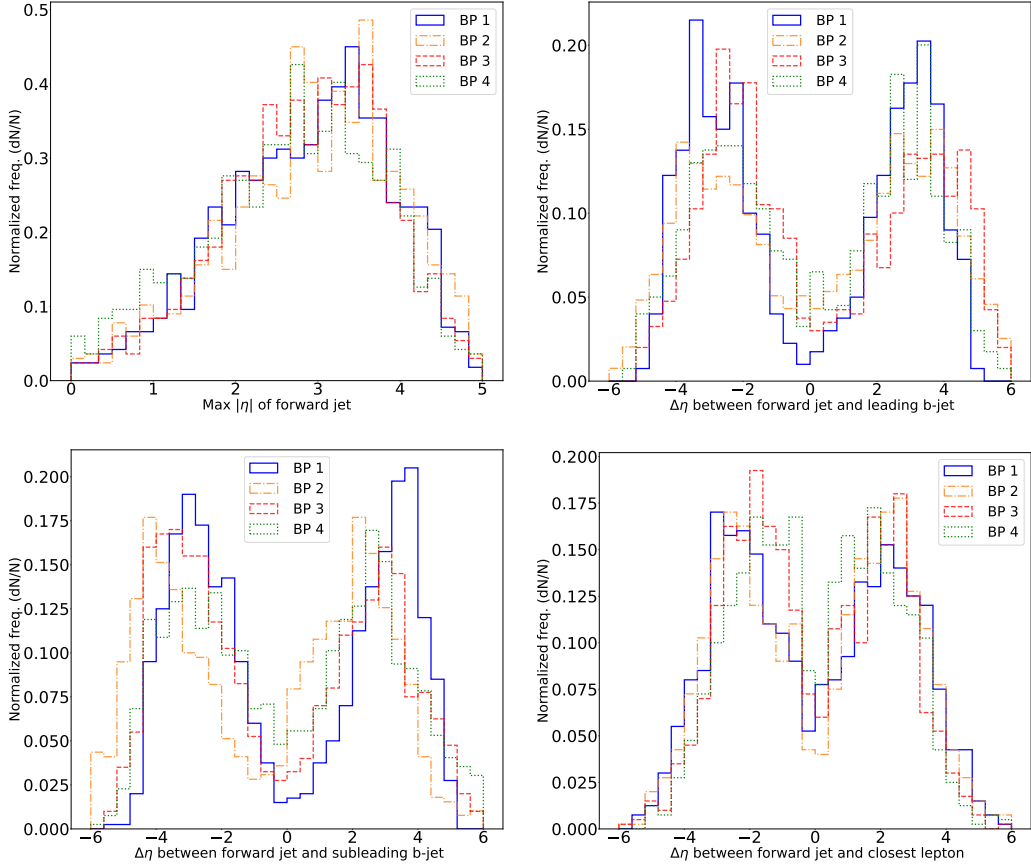


Figure 8. Same as Fig. 7 for different benchmark points BP1-BP4 without the SM background.

Hard Cuts	<ul style="list-style-type: none"> • $\eta_{j_F} > 2.1$ • $\Delta _{j_F b} > 2.0$ • $\Delta _{j_F \ell} > 1.75$.
-----------	---

Table 4. Hard cuts used to segregate thj signal and SM background $t\bar{t}W$ for the SSD events.

with SM and B refers to SM background contribution to SSD events. Note here that z_1 specifically highlights the effect of EFT contribution to the signal, when defined by the difference between signal events produced by EFT operators and that from SM as $S_1 = S - S'$. A priori, such definition may look unphysical, but eventually, all signal events are computed/simulated by some hypothesis and so is this.

We present next in fig. 9 the scan for signal significance z_1 as colour gradient in $C_{4f} - \kappa_t$ plane, for $C_w = 1$ (left) and $C_w = -1$ (right) at $\mathcal{L} = 35.9$ (137) fb^{-1} on the top (bottom) panel. The pattern remains the same as that of fig. 6, understandably because

Cuts	$t\bar{t}W$	thj -SM	BP0	BP1	BP2	BP3	BP4
Basic cuts	199	3.9	44.6	37.7	26.2	4.7	4.0
$ \eta_{j_F} > 2.1$	63	2.8	32.9	27.4	19.4	3.5	3.4
$ \Delta\eta _{j_F b} > 2.0$	28	2.1	25.4	20.7	14.7	3.0	2.4
$ \Delta\eta _{j_F \ell} > 1.75$	18	1.3	20.8	16.9	12.0	2.1	2.3

Table 5. Number of SSD events at LHC resulting from thj production in SM ($\kappa_t = 1$), as well as at benchmark points BP0-BP4, along with $t\bar{t}W$ background with hard cuts applied successively at CM energy $\sqrt{s} = 13$ TeV and $\mathcal{L} = 35.9 \text{ fb}^{-1}$.

Benchmarks	$\{\kappa_t, C_{4f}, C_w\}$	$\sigma_{\text{prod}} \text{ (fb)}$	$N_{\text{basic cuts}}$	$N_{\text{final cut}}$
SM $t\bar{t}h$	$\{1.0, 0, 0\}$	469.3	59.2	11.1
BP0	$\{-1.0, 0, 0\}$	469.8	59.2	11.1
BP1	$\{-1.0, 1.2, 1.0\}$	564.2	71.1	13.4
BP2	$\{-0.5, 1.2, -1.0\}$	141.8	17.9	3.4
BP3	$\{0.5, 0.4, 1.0\}$	121.1	15.3	2.9
BP4	$\{1.0, 0.8, -1.0\}$	513.5	64.7	12.2

Table 6. $t\bar{t}h$ production cross-section, number of SSD signal events after the basic cuts ($N_{\text{basic cuts}}$) and hard cuts ($N_{\text{final cut}}$) for SM and EFT benchmark points BP0-BP4 at LHC with $\sqrt{s} = 13$ TeV and integrated luminosity $\mathcal{L} = 35.9 \text{ fb}^{-1}$.

the signal behaviour remains the same as function of C_{4f}, κ_t , while the background remain unaffected. The white region falls below $2z_1$. With larger luminosity, the white region shrinks and partially comes under discovery/exclusion limit. For example, the point with $\kappa_t = 1$ can get excluded in presence of non-zero $|C_{4f}| \sim 1.5$ with $\mathcal{L} = 137 \text{ fb}^{-1}$. A large portion of $\kappa_t < 0$ can be excluded or discovered in near future. We should also remember that addition of $t\bar{t}h$ contribution to the signal, particularly at the regions of large negative $\kappa_t < 0$ is significant.

4.2 Machine learning techniques

After estimating a maximally achievable signal significance with a simple cut-based analysis, we further explore the possibility of improving the significance by a Machine Learning (ML) technique namely Gradient Boosted Decision Trees (gradient BDT) [37] by employing various kinematical variables. We use the package `XGBoost` [37] as a toolkit for gradient boosting. We use the same ten observables in the CMS analysis [38] as input features for the gradient boosting:

- Number of jets with $p_T > 25 \text{ GeV}$ and $|\eta| < 2.4$,

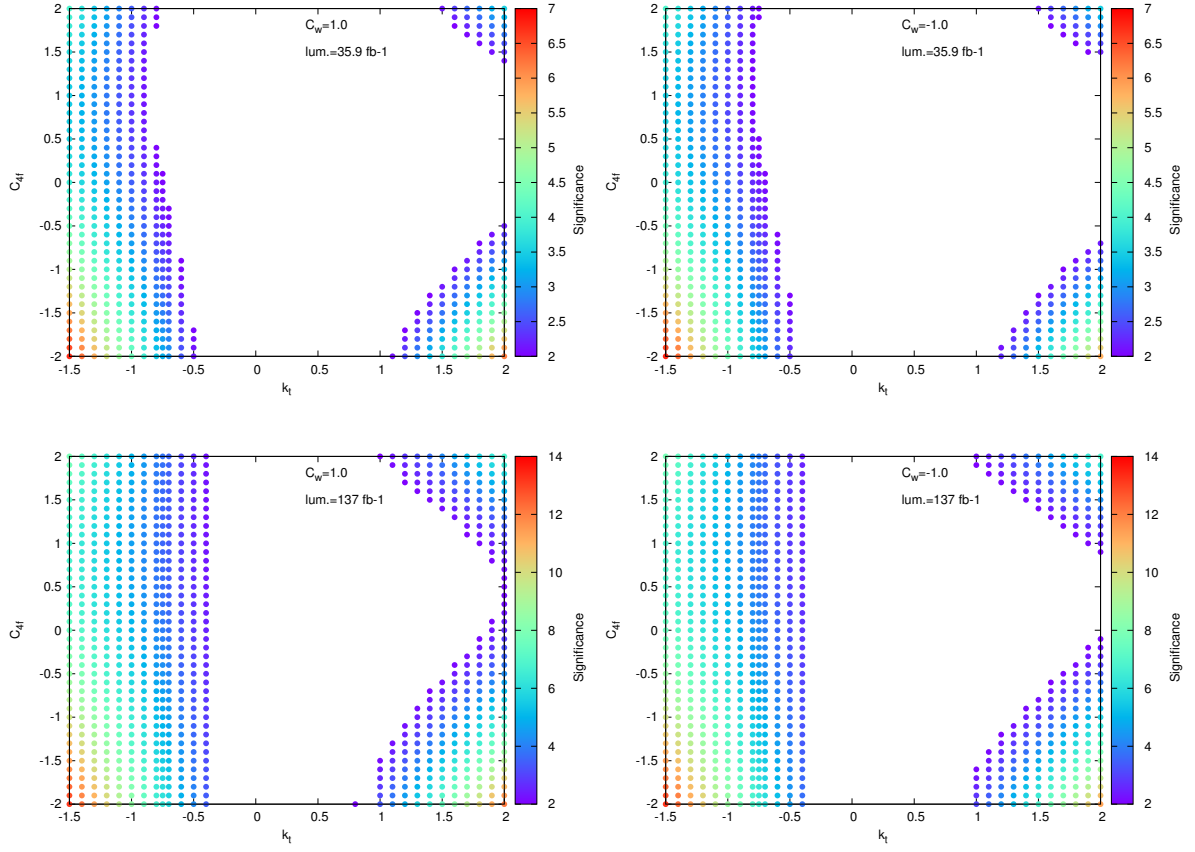


Figure 9. $2z_1$ exclusion plot in $C_{4f} - \kappa_t$ plane with z_1 in colour gradient for constant $C_w = +1$ (left) and $C_w = -1$ (right) for $\mathcal{L} = 35.9$ (137) fb^{-1} on top (bottom) panel at $\sqrt{s} = 13$ TeV LHC. The color gradient marks regions $\geq 2z_1$.

- Maximum $|\eta|$ of the forward jet,
- Sum of lepton charges,
- Number of untagged jets with $|\eta| > 1$,
- $\Delta\eta$ between forward light jet and leading b-tagged jet,
- $\Delta\eta$ between forward light jet and subleading b-tagged jet,
- $\Delta\eta$ between forward light jet and closest lepton,
- $\Delta\Phi$ of highest- p_T same-sign lepton pair,
- Minimum ΔR between the two leptons,
- p_T of sub-leading lepton.

We take an equal number of signal and background events to classify them using the *train* module of **XGBoost**. For the background, $t\bar{t}W$ and $t\bar{t}Z$ events are mixed according to their respective cross-sections. Given the signal distributions are not characteristically different for different choices of κ_t or C_{4f} , C_w (see Fig. 8), signal events from BP1 are used for training while other benchmark points are used for testing purposes. For training the **XGBoost** Classifier, we use 10000 samples each for the signal and background events for BP1 whereas 1000 sample events are used for testing the classifier for all the benchmark points. At first, we use the module **BayesSearchCV** in scikit-optimize [39] library for hyperparameter tuning [40] to obtain a combination of the **XGBoost** parameters that achieves maximum accuracy to classify the signal and the background events. The module utilises Bayesian Optimization [41] where a predictive model referred to as “surrogate” is used to model the search space and utilized to arrive at good parameter values combination as quickly as possible. The optimized parameter values and the corresponding signal efficiencies are listed in tables 7 and 8 respectively. Signal efficiency (background rejection) for all the test benchmark points shows uniformity and averages 75.26 % (75.48 %).

In fig. 10, on the left, we plot the total errors during the training as well as the testing phase as a function of the number of epochs i.e number of runs through the entire dataset whereas on the right we plot the ROC (Receiver Operating Characteristic) curve [42]. The ROC curve is drawn by plotting the true positive rate (TPR) (signal efficiency) against the false positive rate (FPR) (background rejection) at various threshold settings. The true-positive rate is also known as sensitivity, recall, or probability of detection. The false-positive rate is also known as the probability of false alarm and can be calculated as (1 - specificity). The best possible prediction method would yield a point in the upper left corner or coordinate (0,1) of the ROC space, representing 100% sensitivity (no false negatives) and 100% specificity (no false positives). The diagonal line from the bottom left to the top right corners represents random guessing. For the **XGBoost** classifier, all the test points have similar areas under the ROC curves. Also, the difference in the areas between the training and the test curves is not significant suggesting no overfitting of the model.

We calculate the expected Z-value, which is defined as the number of standard deviations from the background-only hypothesis given a signal yield and background uncertainty, using the **BinomialExpZ** function by **RooFit** [43]. We use several values for the relative overall background uncertainty, $\sigma_B = 10\%$, 20% , and 30% with the currently available integrated luminosity of 35.9 fb^{-1} . Clearly, the sensitivity to the NP depends on the relative uncertainty. Keeping that in mind, we analyze all signal channels, assuming that the signal uncertainty is included within σ_B .

Parameter space scan in $C_{4f} - \kappa_t$ plane for SSD signal significance (z) using ML technique with constant $C_w = +1$ (left) and $C_w = -1$ (right) with $\mathcal{L} = 35.9 \text{ fb}^{-1}$ is shown in fig. 11. Darker shades indicate lower signal significance. The pattern is no different than that of fig. 6 or fig. 9 as the signal dependence on the EFT parameters remains the same. We also show constant signal significance (z) contours of one sigma, two sigma etc. by black thick lines, which show larger and larger concentric curves. In the top panel, the SM background error is varied by 10% whereas in the bottom panel the error is varied in a

XGBoost Classifier parameters (variable names)	Optimized values
No. of estimators or trees (n_estimators)	83
Learning rate (η)	0.0521
Maximum depth of a tree: (max_depth)	4.0
Subsample ratio of the training instances (subsample)	0.7565
Subsample ratio of columns when constructing each tree (colsample_bytree)	0.7633
subsample ratio of columns for each level (colsample_bylevel)	0.4436
L2 regularization term on weights (λ)	37.0
L1 regularization term on weights (α)	3.0
Minimum loss reduction required to make a further partition on a leaf node (γ)	3.607
Minimum sum of instance weight (hessian) needed in a child (min_child_weight)	71.0
Maximum delta step allowed for each leaf output to be. (max_delta_step)	4.0

Table 7. Optimized parameter values for the XGBoost Classifier tuned using Bayesian Hyperparameter Optimization. The rest of the parameters are set to default options.

	<i>thj</i> -SM	BP0	BP1	BP2	BP3	BP4
N_{bc}	3.9	47.6	39.0	26.46	4.38	6.01
XGBoost						
Signal Efficiency	69.8%	81.0%	89.5%	76.8%	74.9%	73.8%
Background Rejection	75.4%	75.4%	80.8%	74.5%	73.8%	78.3%

Table 8. Comparison of signal efficiency and background rejection for all the benchmark points and SM-*thj*. The results are obtained using a test dataset of 1000 signal and background events after training the XGBoost classifier on 10000 events from BP1.

larger range 30%. Obviously, this results in smaller significance in lower panel figures, i.e. one sigma significance is achieved for larger values of C_{4f}, κ_t .

\mathcal{L}	35.9 fb ⁻¹				140 fb ⁻¹			
z	2	3	4	5	2	3	4	5
$\kappa_t = -1.0$	[0.2, 2.004]	[-1.45, 3.51]	[-2.44, -]	[-3.25, -]	*	*	[0.86, 1.38]	[-0.50, 2.62]
$\kappa_t = 1.0$	[-2.87, 2.96]	[-3.57, 3.64]	-	-	[-1.24, 1.35]	[-1.70, 1.80]	[-2.07, 2.16]	[-2.39, 2.46]
$\kappa_t = 1.5$	[-1.76, 2.17]	[-2.27, 2.62]	[-2.69, 3.0]	[-3.07, 3.33]	[-0.55, 1.06]	[-0.93, 1.40]	[-1.22, 1.66]	[-1.47, 1.87]
$\kappa_t = 2.2$	[-0.88, 1.57]	[-1.30, 1.93]	[-1.65, 2.22]	[-1.96, 2.46]	*	[0.0, 0.80]	[-0.37, 1.44]	[-0.63, 1.37]

Table 9. Exclusion limits on C_{4f} for different values of κ_t using $C_w = +1$ using ML techniques at $\sqrt{s} = 13$ TeV LHC for $\mathcal{L} = 35.9, 140$ fb⁻¹. The - sign indicates the breakdown of the EFT limit whereas * shows no feasible region in the $\kappa_t - C_{4f}$ plane.

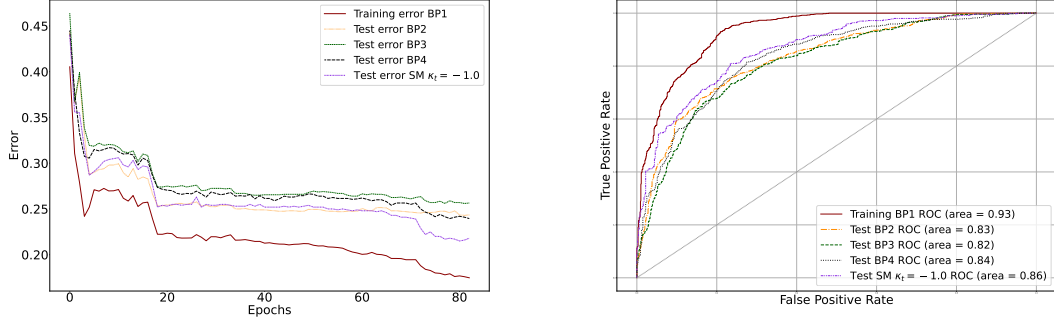


Figure 10. Change in loss function with the number of epochs for all the benchmark points (left) and corresponding performance in terms of ROC (receiver operating characteristic) for the `XGBoostClassifier` (right). One epoch is a single run through the entire dataset.

We then quote the exclusion limits on C_{4f} for constant κ_t with a constant $C_w = +1$, for different luminosities in Table 9 that result from ML-based analysis. For example, with $\kappa_t = -1.0$, we see that the C_{4f} can acquire values 0.2 and 2.004 when the signal receives 2σ significance. This is again attributed to both the interference as well as the quadratic contribution of the Wilson coefficient. Usually, the points within the quoted maximum limits of C_{4f} provides a lower signal significance with constant κ_t . The $-$ sign indicates very large values of Wilson coefficients where EFT limit breaks down, and $*$ shows no feasible region in the $\kappa_t - C_{4f}$ plane.

5 Summary and Conclusions

In this work, we analyze the single top associated with Higgs production to estimate the limit on top Higgs Yukawa coupling (κ_t) at the LHC in the current and upcoming sensitivities using run-2 data corresponding to $\sqrt{s} = 13$ TeV, including SM effective operator contributions upto dimension six. All the operators that can contribute to such signal have been considered, taking into account limits on such operators from other observables. We see that the most significant contribution comes from the four fermi operators $\mathcal{O}_{qq}^{(1)}, \mathcal{O}_{qq;1}^{(3)}, \mathcal{O}_{qq;2}^{(3)}$. Apart, the operator $\mathcal{O}_{\phi q}^{(3)}$ also contributes, but the effect is much milder. We neglect other LG operators as their contributions are suppressed. Together, the Wilson coefficient of four fermi operator and the variable Yukawa coupling $\{C_{4f}, \kappa_t\}$ serve as the major NP parameters of the framework. The other parameter, NP scale is kept fixed at $\Lambda = 1$ TeV. The effective field theory (EFT) description is validated with M_{tj} invariant mass distribution peaking at a much lower value than the chosen NP scale $\Lambda = 1$ TeV.

The possible types of heavy physics that generate four fermi operator of the kind $(\bar{d}_L \gamma_\mu u_L)(\bar{t}_L \gamma^\mu b_L)$ that contributes to thj production at LHC have also been chalked out. Importantly we point out that the NP that contributes potentially to $qb \rightarrow q't$, has a

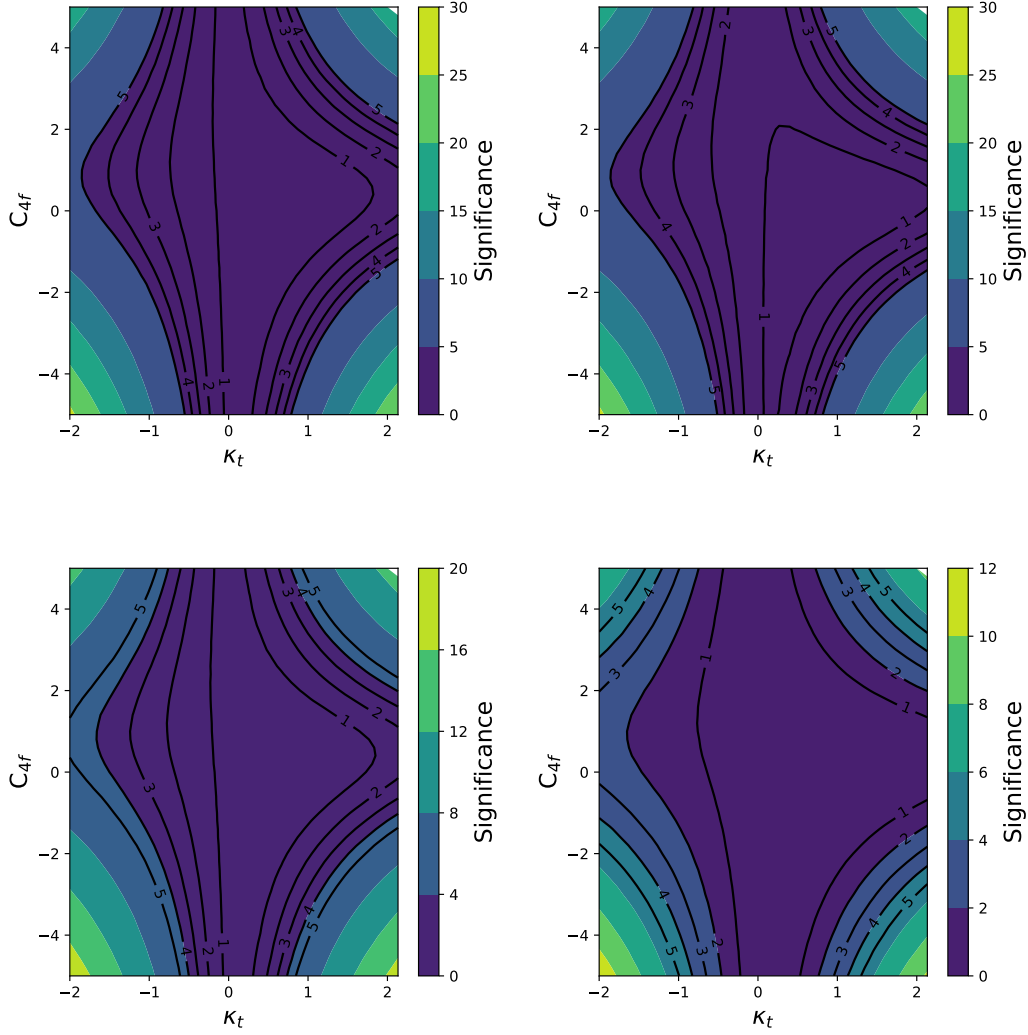


Figure 11. Plots with SSD signal significance (z) in colour gradient in $C_{4f} - \kappa_t$ plane for constant $C_w = +1$ (left) and $C_w = -1$ (right) constant luminosity 35.9 fb^{-1} at $\sqrt{s} = 13 \text{ TeV}$ LHC. Constant significance lines are also shown by black thick lines. SM Error has been varied by 10% in the top panel and 30 % in the bottom panel.

negligible contribution to $qq' \rightarrow t\bar{b}$. Thus the omission of $qq' \rightarrow t\bar{b}$ to our signal, in presence of untagged b jet is justified.

The key variables that distinguish the signal events from the $t\bar{t}W/t\bar{t}Z$ background include $|\eta|$ of the forward jet, pseudorapidity difference $(\Delta\eta)_{j_F b}$ between forward jet with both leading and sub-leading b jets, and pseudorapidity difference $\Delta\eta_{\ell j_F}$ between lepton and forward jet. The kinematic distributions in presence of the EFT contribution do not significantly differ from the corresponding SM ones. An optimised choice of hard cuts on

these variables retain signal and provide 5σ discovery reach for the future luminosities. The same analysis is done with ML technique, which is consistent with the cut-based analysis.

We see that in presence of $\{C_{4f}, C_w\}$, the limit on κ_t gets stronger for $C_{4f} < 0$ and relaxed for $C_{4f} > 0$. We also observe an asymmetry in the dependence on C_{4f} for $\kappa_t > 0$, which indicates to a potential contribution proportional to C_{4f}^2 beyond the interference term with SM. For SM like case with $\kappa_t = 1$, 3σ significance can be achieved for both values of $[C_{4f}] = [-2.69, 2.75]$ when $C_w = +1$, while for $\kappa_t = -1$, the same is achieved for much lower values of $[C_{4f}] = [0.82, 1.42]$ at integrated luminosity 140 fb^{-1} . Thus the limits obtained on κ_t in absence of EFT operator coefficients like C_{4f} are significantly different, making it a necessity to consider them for future analysis of thj process at the LHC.

Acknowledgments: Subhadiya acknowledges to the Core Research Grant support CRG/2019/004078 from DST-SERB, Govt. of India. Sanjoy would like to thank Shivam Verma for various technical helps. We would also like to thank Prof. Kajari Mazumdar and Pallabi Das for important clarifications on experimental analysis.

References

- [1] **Particle Data Group** Collaboration, R. L. Workman and Others, *Review of Particle Physics*, *PTEP* **2022** (2022) 083C01.
- [2] K.-P. Xie and B. Yan, *Probing the electroweak symmetry breaking with Higgs production at the LHC*, *Phys. Lett. B* **820** (2021) 136515, [[arXiv:2104.12689](#)].
- [3] **CMS** Collaboration, A. M. Sirunyan et al., *Measurements of $t\bar{t}H$ Production and the CP Structure of the Yukawa Interaction between the Higgs Boson and Top Quark in the Diphoton Decay Channel*, *Phys. Rev. Lett.* **125** (2020), no. 6 061801, [[arXiv:2003.10866](#)].
- [4] S. Biswas, E. Gabrielli, and B. Mele, *Single top and Higgs associated production as a probe of the Htt coupling sign at the LHC*, *JHEP* **01** (2013) 088, [[arXiv:1211.0499](#)].
- [5] M. Farina, C. Grojean, F. Maltoni, E. Salvioni, and A. Thamm, *Lifting degeneracies in Higgs couplings using single top production in association with a Higgs boson*, *JHEP* **05** (2013) 022, [[arXiv:1211.3736](#)].
- [6] S. Banerjee, R. S. Gupta, J. Y. Reiness, S. Seth, and M. Spannowsky, *Towards the ultimate differential SMEFT analysis*, *JHEP* **09** (2020) 170, [[arXiv:1912.07628](#)].
- [7] **CMS** Collaboration, A. M. Sirunyan et al., *Search for associated production of a Higgs boson and a single top quark in proton-proton collisions at $\sqrt{s} = 13 \text{ TeV}$* , *Phys. Rev. D* **99** (2019), no. 9 092005, [[arXiv:1811.09696](#)].
- [8] J. Alwall, M. Herquet, F. Maltoni, O. Mattelaer, and T. Stelzer, *MadGraph 5 : Going Beyond*, *JHEP* **06** (2011) 128, [[arXiv:1106.0522](#)].
- [9] B. Grzadkowski, M. Iskrzynski, M. Misiak, and J. Rosiek, *Dimension-Six Terms in the Standard Model Lagrangian*, *JHEP* **10** (2010) 085, [[arXiv:1008.4884](#)].
- [10] M. B. Einhorn and J. Wudka, *The Bases of Effective Field Theories*, *Nucl. Phys. B* **876** (2013) 556–574, [[arXiv:1307.0478](#)].
- [11] F. Maltoni, L. Mantani, and K. Mimasu, *Top-quark electroweak interactions at high energy*, *JHEP* **10** (2019) 004, [[arXiv:1904.05637](#)].

- [12] H. E. Faham, F. Maltoni, K. Mimasu, and M. Zaro, *Single top production in association with a WZ pair at the LHC in the SMEFT*, *JHEP* **01** (2022) 100, [[arXiv:2111.03080](#)].
- [13] C. Degrande, F. Maltoni, K. Mimasu, E. Vryonidou, and C. Zhang, *Single-top associated production with a Z or H boson at the LHC: the SMEFT interpretation*, *JHEP* **10** (2018) 005, [[arXiv:1804.07773](#)].
- [14] M. Guchait and A. Roy, *Exploring SMEFT operators in the tHq production at the LHC*, [arXiv:2210.05503](#).
- [15] Q.-H. Cao, H.-r. Jiang, and G. Zeng, *Single top quark production with and without a Higgs boson*, *Chin. Phys. C* **45** (2021), no. 9 093110, [[arXiv:2105.04464](#)].
- [16] C. Arzt, *Reduced effective Lagrangians*, *Phys. Lett. B* **342** (1995) 189–195, [[hep-ph/9304230](#)].
- [17] M. B. Einhorn and J. Wudka, *Higgs-Boson Couplings Beyond the Standard Model*, *Nucl. Phys. B* **877** (2013) 792–806, [[arXiv:1308.2255](#)].
- [18] **CMS** Collaboration, V. Khachatryan et al., *Search for anomalous Wtb couplings and flavour-changing neutral currents in t-channel single top quark production in pp collisions at $\sqrt{s} = 7$ and 8 TeV*, *JHEP* **02** (2017) 028, [[arXiv:1610.03545](#)].
- [19] **CMS** Collaboration, A. M. Sirunyan et al., *Measurement of CKM matrix elements in single top quark t-channel production in proton-proton collisions at $\sqrt{s} = 13$ TeV*, *Phys. Lett. B* **808** (2020) 135609, [[arXiv:2004.12181](#)].
- [20] A. Kozachuk and D. Melikhov, *Constraints on the anomalous Wtb couplings from B-physics experiments*, *Symmetry* **12** (2020), no. 9 1506, [[arXiv:2004.13127](#)].
- [21] A. Buckley, C. Englert, J. Ferrando, D. J. Miller, L. Moore, M. Russell, and C. D. White, *Constraining top quark effective theory in the LHC Run II era*, *JHEP* **04** (2016) 015, [[arXiv:1512.03360](#)].
- [22] S. Stamm, *Combined Measurement of Single Top-Quark Production in the s and t-Channel with the ATLAS Detector and Effective Field Theory Interpretation*. PhD thesis, Humboldt U., Berlin, 2018.
- [23] A. Alloul, N. D. Christensen, C. Degrande, C. Duhr, and B. Fuks, *FeynRules 2.0 - A complete toolbox for tree-level phenomenology*, *Comput. Phys. Commun.* **185** (2014) 2250–2300, [[arXiv:1310.1921](#)].
- [24] S. Bhattacharya and J. Wudka, *Dimension-seven operators in the standard model with right handed neutrinos*, *Phys. Rev. D* **94** (2016), no. 5 055022, [[arXiv:1505.05264](#)]. [Erratum: *Phys.Rev.D* **95**, 039904 (2017)].
- [25] F. Maltoni, G. Ridolfi, and M. Ubiali, *b-initiated processes at the LHC: a reappraisal*, *JHEP* **07** (2012) 022, [[arXiv:1203.6393](#)]. [Erratum: *JHEP* **04**, 095 (2013)].
- [26] **NNPDF** Collaboration, R. D. Ball et al., *Parton distributions for the LHC Run II*, *JHEP* **04** (2015) 040, [[arXiv:1410.8849](#)].
- [27] S. Mrenna and P. Skands, *Automated Parton-Shower Variations in Pythia 8*, *Phys. Rev. D* **94** (2016), no. 7 074005, [[arXiv:1605.08352](#)].
- [28] M. L. Mangano, M. Moretti, F. Piccinini, and M. Treccani, *Matching matrix elements and shower evolution for top-quark production in hadronic collisions*, *JHEP* **01** (2007) 013, [[hep-ph/0611129](#)].

- [29] **DELPHES 3** Collaboration, J. de Favereau, C. Delaere, P. Demin, A. Giammanco, V. Lemaitre, A. Mertens, and M. Selvaggi, *DELPHES 3, A modular framework for fast simulation of a generic collider experiment*, *JHEP* **02** (2014) 057, [[arXiv:1307.6346](#)].
- [30] M. Cacciari, G. P. Salam, and G. Soyez, *The anti- k_t jet clustering algorithm*, *JHEP* **04** (2008) 063, [[arXiv:0802.1189](#)].
- [31] M. Cacciari, G. P. Salam, and G. Soyez, *FastJet User Manual*, *Eur. Phys. J. C* **72** (2012) 1896, [[arXiv:1111.6097](#)].
- [32] M. Cacciari and G. P. Salam, *Dispelling the N^3 myth for the k_t jet-finder*, *Phys. Lett. B* **641** (2006) 57–61, [[hep-ph/0512210](#)].
- [33] **ATLAS** Collaboration, *Expected performance of the ATLAS b-tagging algorithms in Run-2*, .
- [34] **CMS** Collaboration, A. M. Sirunyan et al., *Measurement of the cross section for top quark pair production in association with a W or Z boson in proton-proton collisions at $\sqrt{s} = 13$ TeV*, *JHEP* **08** (2018) 011, [[arXiv:1711.02547](#)].
- [35] **CMS** Collaboration, *Search for new physics using effective field theory in 13 TeV pp collision events that contain a top quark pair and a boosted Z or Higgs boson*, [arXiv:2208.12837](#).
- [36] **SMEFiT** Collaboration, J. J. Ethier, G. Magni, F. Maltoni, L. Mantani, E. R. Nocera, J. Rojo, E. Slade, E. Vryonidou, and C. Zhang, *Combined SMEFT interpretation of Higgs, diboson, and top quark data from the LHC*, *JHEP* **11** (2021) 089, [[arXiv:2105.00006](#)].
- [37] T. Chen and C. Guestrin, *Xgboost: A scalable tree boosting system*, in *Proceedings of the 22nd acm sigkdd international conference on knowledge discovery and data mining*, pp. 785–794, 2016.
- [38] R. K. Barman, D. Gonçalves, and F. Kling, *Machine learning the higgs boson-top quark cp phase*, *Phys. Rev. D* **105** (Feb, 2022) 035023.
- [39] G. L. Iaroslav Shcherbatyi, Tim Head and H. Nahrstaedt, *Scikit-learn hyperparameter search wrapper*, 2017.
- [40] M. Claesen and B. De Moor, *Hyperparameter search in machine learning*, *arXiv preprint arXiv:1502.02127* (2015).
- [41] R. Garnett, *Bayesian Optimization*. Cambridge University Press, 2022. in preparation.
- [42] T. Fawcett, *An introduction to roc analysis*, *Pattern Recogn. Lett.* **27** (jun, 2006) 861–874.
- [43] W. Verkerke and D. P. Kirkby, *The RooFit toolkit for data modeling*, *eConf C0303241* (2003) MOLT007, [[physics/0306116](#)].